NREL/TP-471-5543 • UC Category: 237 • DE94000267

CATARACT - Computer Code for Improving Power Calculations at NREL's High-Flux Solar Furnace

Kent Scholl
Carl Bingham
Allan Lewandowski

Prepared for the 1994 ASME/JSME/JSES International Solar Energy Conference, San Francisco, California, March 27-30, 1994

National Renewable Energy Laboratory
1617 Cole Boulevard
Golden, Colorado 80401-3393
A national laboratory of the U.S. Department of Energy
Operated by the Midwest Research Institute
for the U.S. Department of Energy
under Contract No. DE-AC02-83CH10093

January 1994

NOTICE

Printed in the United States of America
Available from:
National Technical Information Service
U.S. Department of Commerce
5285 Port Royal Road
Springfield, VA 22161

Price: Microfiche A01
Printed Copy A02

Codes are used for pricing all publications. The code is determined by the number of pages in the publication. Information pertaining to the pricing codes can be found in the current issue of the following publications which are generally available in most libraries: *Energy Research Abstracts (ERA)*; *Government Reports Announcements and Index (GRA and I)*; *Scientific and Technical Abstract Reports (STAR)*; and publication NTIS-PR-360 available from NTIS at the above address.


Printed on recycled paper

CATARACT - COMPUTER CODE FOR IMPROVING POWER CALCULATIONS AT NREL's HIGH-FLUX SOLAR FURNACE

Kent Scholl, Carl Bingham, and Allan Lewandowski
National Renewable Energy Laboratory
1617 Cole Blvd.
Golden, Colorado 80401

ABSTRACT

The High-Flux Solar Furnace (HFSF), operated by the National Renewable Energy Laboratory, uses a camera-based, flux-mapping system to analyze the flux distribution and to determine total power at the focal point. The flux-mapping system consists of a diffusely reflecting plate with seven circular foil calorimeters, a charge-coupled device (CCD) camera, an IBM-compatible personal computer with a frame-grabber board, and commercial image analysis software. The calorimeters provide flux readings that are used to scale the image captured from the plate by the camera. The image analysis software can estimate total power incident on the plate by integrating under the 3-dimensional image.

Because of the physical layout of the HFSF, the camera is positioned at a 20° angle to the flux mapping plate normal. The foreshortening of the captured images that results represents a systematic error in the power calculations because the software incorrectly assumes the image is parallel to the camera's array.

We have written a FORTRAN computer program called CATARACT (CAmera/TARget Angle CorrecTion) that we use to transform the original flux-mapper image to a plane that is normal to the camera's optical axis. A description of the code and the results of experiments performed to verify it are presented. Also presented are comparisons of the total power available from the HFSF as determined from the flux mapping system and theoretical considerations.

NOMENCLATURE

$\hat{A}$ - a ray from the camera to the transform plane
A - area, m^2
D - distance from the camera's array to the focal point, cm
Q - direct normal solar intensity, kW/m^2
SF - BEAMCODE ScaleFactor parameter
x - horizontal location, cm
y - vertical location, cm
α - angle between the camera's optical axis and a horizontal location on the transform plane
β - angle between the camera's optical axis and a vertical location on the transform plane
θ - angle between the target plane and the transform plane

Subscripts
c - concentrator
h - heliostat
i - horizontal pixel location on CCD array
j - vertical pixel location on CCD array
sw - solar weighted

Superscripts
' - position on the target plane
" - position on the transform plane

INTRODUCTION

The High-Flux Solar Furnace (HFSF) is a 10-kW solar concentrator that is designed with the focal point 28° off of the heliostat-to-primary concentrator axis (Lewandowski, 1989). Peak concentrations at the focal point from the primary concentrators are about 2400 times greater than incident sunlight. Because of the off-axis design, the furnace has a focal-length-to-diameter ratio of 1.85, which is higher than most solar furnaces. This large focal-length to diameter ratio allows the use of secondary concentrators to achieve concentration ratios over 21,000 (Lewandowski, et al., 1991).

Currently, the flux distribution and total power available from the furnace's primary concentrator are analyzed with a scatter-plate flux-mapping system (Masterson and Bohn, 1982). Our scatter-plate system consists of a diffusely reflecting plate, a charge-couple device (CCD) camera, a personal computer with a

TABLE 1. COMPARISON OF POWER DELIVER TO THE HFSF TARGET PLAIN AS DETERMINED FROM THEORETICAL CALCULATIONS AND THE FLUX-MAPPING SYSTEM, WITH AND WITHOUT THE USE OF THE CATARACT CODE.

Test Number	Theoretical Power (kW)	BEAMCODE Power w/o CATARACT (kW)	BEAMCODE Power with CATARACT (kW)	Percent Difference w/o CATARACT Processing	Percent Difference with CATARACT Processing
1	8.35	8.08	8.50	-3.2%	1.8%
2	8.36	8.07	8.52	-3.5%	1.9%

frame-grabber board, and image analysis software (Bingham and Lewandowski, 1991). The flux-mapping target we use at the HFSF is a water-cooled aluminum plate coated with Eastman Kodak 6080 White Reflectance Coating. One half of the plate is a bare, diffusely reflecting surface from which we capture images; the other half of the plate contains seven circular foil calorimeters. The calorimeters provide flux readings that we use to scale the captured image.

We use commercial laser-diagnostic software called BEAMCODE (Big Sky Laser Technology, Inc.) to analyze the flux-mapper images captured by a COHU 4815 camera. The images are stored as a 240x240 grid of digital intensity data; resolution is 8 bits. Using the flux readings from the calorimeters to scale the camera intensity, the software can integrate under the three-dimensional image to estimate total power. The system provides a relatively quick and simple method to obtain flux distributions and total power estimates.

Because of the HFSF's off-axis design and long focal length, it is not possible to position the camera along the concentrator's optical axis. Thus, the camera's array is not parallel to the target plane. Images captured by the camera do not display their true shape. As a result, flux distribution and total power calculations contain a systematic measurement error.

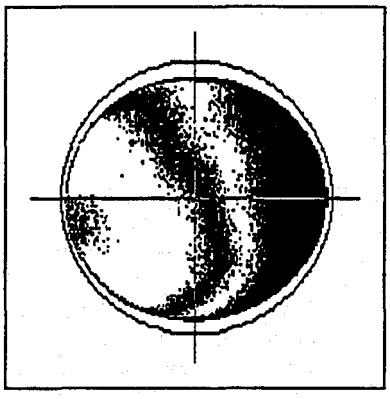

FIGURE 1. IMAGE OF A DIFFUSE, CIRCULAR TARGET WITH THE CAMERA POSITIONED AT A 20° ANGLE. THE OUTER CIRCLE HAS BEEN SUPERIMPOSED ON THE IMAGE.

To demonstrate the effect, a sample target was made of a white, highly diffuse circle with an 8.9 cm diameter on a flat-black background. An electric lamp was positioned to one side of the target to provide sufficient illumination. Figure 1 is an image of the target with the camera positioned at 20°. The image is surrounded by a 9.5 cm diameter circle. The foreshortening of the image is readily obvious.

We felt it should be possible to correct for this systematic error by employing a computer routine to correct the digital data of the captured image. Conceptually, we wanted to rotate the target plane to a position that is normal to the camera. Next, we could map the data on the now irregularly spaced grid of the rotated target plane onto a regularly spaced grid. Finally, the corrected image could then be loaded into BEAMCODE for power and flux distribution analysis.

SYSTEM GEOMETRY

Figure 2 shows the geometry of our flux-mapping system. The camera is located at the intersection of the X and Y axes; the Z axis is the camera's optical axis. The target plane is inclined at an angle θ to the transform plane, which is the plane at the focal point normal to the camera. D is the distance from the camera to the focal point. A-A represents a line through the focal point parallel to the X-axis. We assign a ray, $\hat{A}_{ij}$, that connects any camera pixel (i,j) to its corresponding location on the transform plane, (x''_i, y''_j), shown as point P_2. $\hat{A}_{ij}$ intercepts the target plane at a location (x'_{ij}, y'_j), shown in the figure as point P_1.

The horizontal pixel spacing on the camera's array is 23 μm; the vertical spacing is 27 μm. BEAMCODE uses a ScaleFactor parameter, SF, to scale the image so as to present it with the correct dimensions.

The horizontal location on the camera, x_i, as shown in Figure 3, is defined as:

$$x_i = 0.0023\,\text{cm} * (120.5 - i). \quad (1)$$

The value of i ranges from 1 to 240.

The horizontal location on the transform plane, x_i'', is defined as:

$$x_i'' = SF * 0.0023\,\text{cm} * (120.5 - i). \quad (2)$$

The angle α_i, D, x_i, and x_i'' are related by

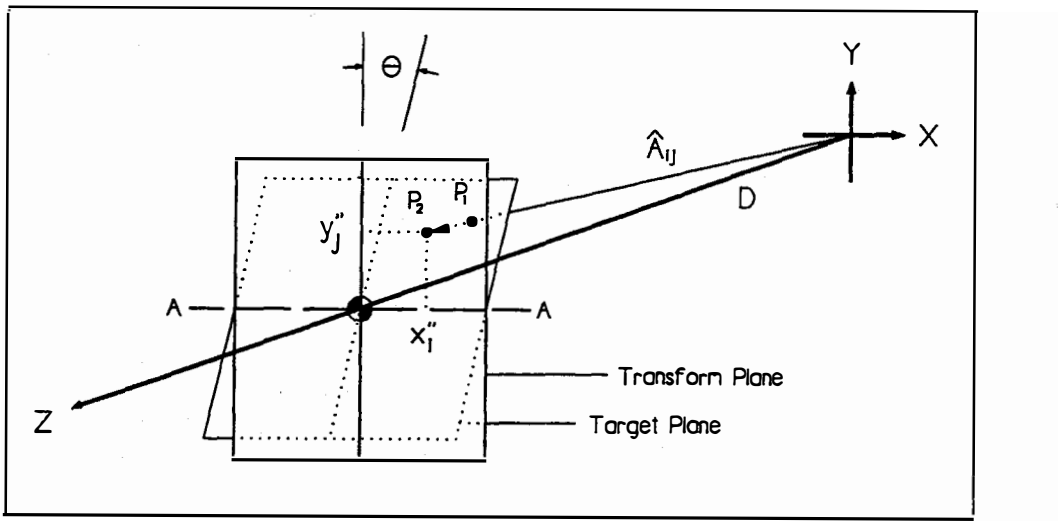

FIGURE 2. PHYSICAL GEOMETRY OF THE FLUX-MAPPING SYSTEM.

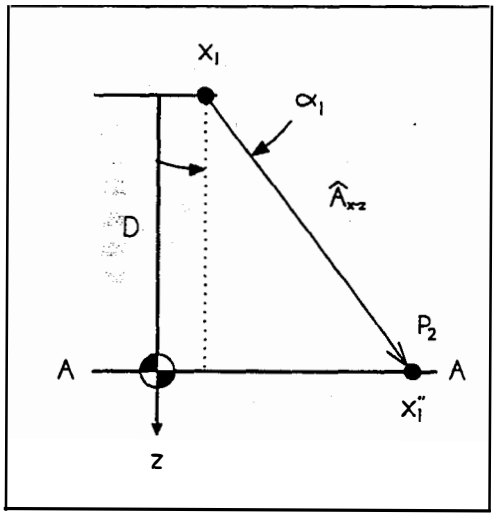

FIGURE 3. DIAGRAM FOR THE DETERMINATION OF α_I. $\hat{A}_{X\text{-}Z}$ IS THE PROJECTION OF THE RAY $\hat{A}_{IJ}$.

$$\tan\alpha_i = \frac{x_i'' - x_i}{D}. \tag{3}$$

Combining Eqs. 1, 2, and 3, we can derive an equation for α_i, the horizontal angle of the projection of $\hat{A}_{ij}$ in the X-Z plane:

$$\alpha_i = \tan^{-1}\left(\frac{(SF-1)}{D} \cdot 0.0023\,\text{cm} \cdot (120.5-i)\right). \tag{4}$$

In a completely analogous way, we can derive an equation for β_j, the vertical angle of the projection of $\hat{A}_{ij}$ in the Y-Z plane:

$$\beta_j = \tan^{-1}\left(\frac{(SF-1)}{D} \cdot 0.0027\,\text{cm} \cdot (120.5-j)\right). \tag{5}$$

The value of j also ranges from 1 to 240.

Figure 4 is a view of the Y-Z plane. From it, the following relations between β_j, D, and y''_j and between β_j, θ, D, and y'_j can be derived:

$$y_j'' = D\tan\beta_j, \tag{6}$$

$$\tan\beta_j = \frac{y_j'\cos\theta}{D - y_j'\sin\theta}. \tag{7}$$

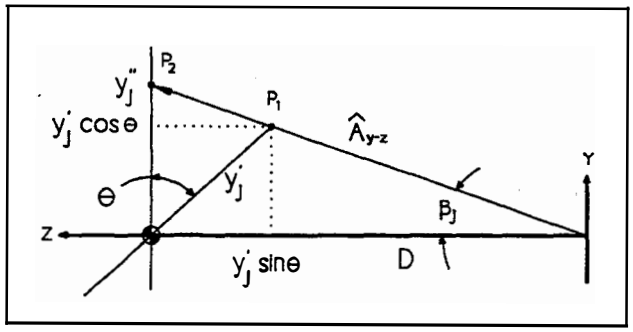

FIGURE 4. VIEW OF THE Y-Z PLANE. $\hat{A}_{Y\text{-}Z}$ IS THE PROJECTION OF THE RAY $\hat{A}_{IJ}$.

Solving for y'_j,

$$y_j' = D \tan\beta_j \left(\frac{1}{\cos\theta + \tan\beta_j \sin\theta} \right). \quad (8)$$

Figure 5 is a view of the X-Z plane. From it, the following relations between α_i, D, and x''_i and between α_i, θ, D, x'_{ij}, and y'_j can be derived:

$$x_i'' = D \tan\alpha_i, \quad (9)$$

$$\tan\alpha_i = \frac{x_{ij}'}{D - y_j' \sin\theta} \quad (10)$$

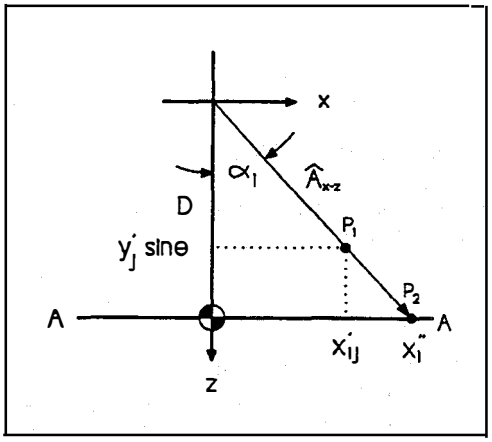

FIGURE 5. VIEW OF THE X-Z PLANE. $\hat{A}_{X-Z}$ IS THE PROJECTION OF THE RAY $\hat{A}_{ij}$.

Substituting Eq. 8 into Eq. 10, the following relation for x'_{ij} can be determined:

$$x_{ij}' = D \tan\alpha_i \left(\frac{1}{1 + \tan\beta_j \tan\theta} \right). \quad (11)$$

CATARACT COMPUTER CODE

Given Eqs. 4, 5, 6, 8, 9, and 11, we have enough information to perform the transformation. The CATARACT program traces the following steps:

1) Read the pixel intensity data and ScaleFactor parameter from the BEAMCODE file.

2) For i = 1,240, determine α_i from Eq. 4.

3) For j = 1,240, determine β_j from Eq. 5.

Map the information from the rotated target plane to the transform plane. For every pixel (i,j):

4) Determine which block of four points, (x'_{ij}, y'_j as determined from Eqs. 8 and 11), on the rotated target plane encompasses the point (x''_i,y''_j) on the transform plane.

5) Perform a bilinear interpolation between the four target plane points to determine the digital pixel intensity at point (x''_i,y''_j).

6) Write the new pixel intensity data to the BEAMCODE file.

RESULTS OF THE CATARACT CODE

Figure 6 is an image displayed within BEAMCODE of the data shown previously in Figure 1, but after processing the image through CATARACT. The circle surrounding the image is 9.5 cm in diameter. As indicated by the circular shape of the image, the code is correctly remapping the intensity data to the correct positions.

We captured a series of images of the diffuse white circle with the camera at an angle ranging from 0 to 25°. The black background of the target, however, was not entirely diffuse. In order to diminish the effects of the background specularity, any pixel intensity that was less than 10% of the peak intensity was set to zero.

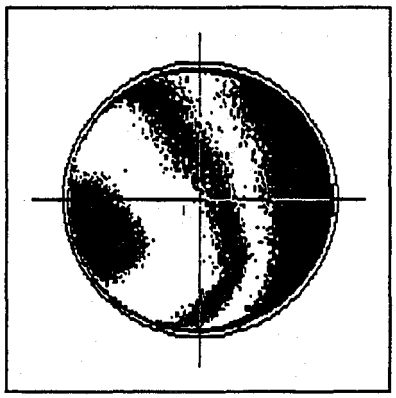

FIGURE 6. IMAGE SHOWN PREVIOUSLY IN FIGURE 1 AFTER PROCESSING THROUGH THE CATARACT CODE.

The calculated power of the images taken at 0° were averaged to an arbitrary value of 1.00 within the BEAMCODE program. The images collected at the various angles were then compared to the 0° images to determine their apparent power levels. The results both before and after CATARACT processing are shown in Figure 7. The small amount of scatter in the transformed data about the 1.00 line is most likely due to small fluctuations in the lamp output, inaccurate positioning of the camera relative to the target, and some non-diffuse characteristics of the target.

POWER CALCULATIONS AT THE HFSF

Total power calculations from the flux-mapping system can be compared to power estimates based on theoretical calculations. For the HFSF, theory predicts that the total amount of energy

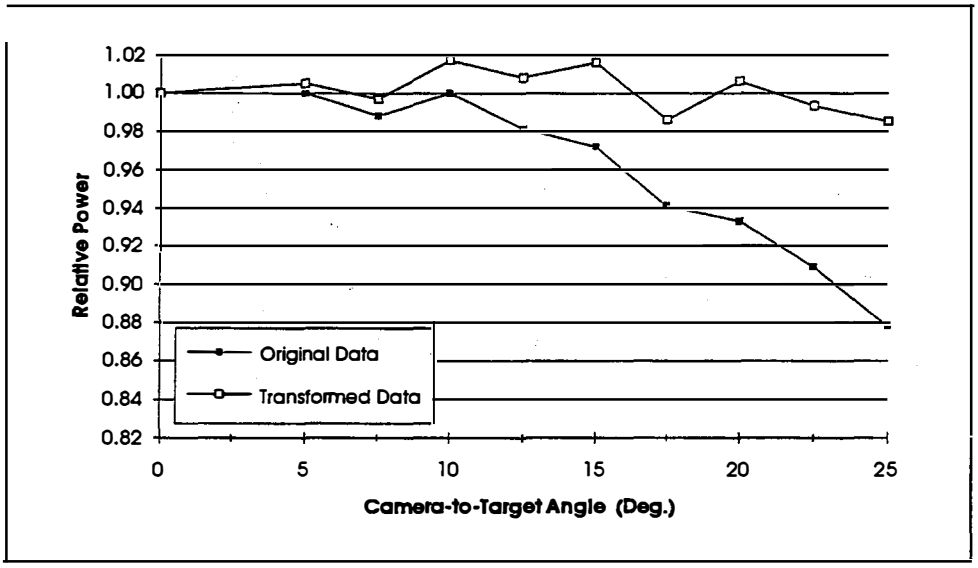

FIGURE 7. RESULTS OF THE CAMERA-TO-TARGET ANGLE TEST BEFORE AND AFTER PROCESSING THE IMAGES THROUGH THE CATARACT CODE.

reaching the target plane should be equal to the product of the direct normal incident sunlight, Q, the concentrator surface area normal to the heliostat, A_c*cos14°, and the solar-weighted reflectivities of the mirror surfaces, $\rho_{h,sw}$ and $\rho_{c,sw}$.

The HFSF's heliostat panels have been exposed to the elements for 4 years; visible deterioration is evident. Recently, the reflectivity of the heliostat panels was measured with a portable Devices & Services (D&S) reflectometer. This instrument uses a small laser to measure the specular reflectivity at 650 nm. Previously, we had estimated the solar-weighted reflectivity of the heliostat by comparing the current measurements at 650 nm to those of measurements at 650 nm on pristine panels of known solar-weighted reflectivity. The problem with this approach is that the heliostat mirrors may not be degrading in a gray fashion; the reductions in reflectivity at 650 nm may not be representative of the reflectivity at all wavelengths of solar radiation.

We have also measured the reflectivity of some of the heliostat panels using a Gier Dunkle Mobile Solar Reflectometer. This device uses a xenon lamp and an integrating sphere to directly give an estimate of solar-weighted reflectivity. Unfortunately, the speed of the device is quite slow and, because of its design, can only reach the outer panels of the heliostat. However, because the readings from the Gier Dunkle device are in good agreement with mirror samples of known reflectivity, we have used the ratio between the Gier Dunkle and the D&S measurements on a few heliostat panels to more accurately estimate the solar weighted reflectivity of the entire heliostat. Using this approach, we assign a value of 83.5% to $\rho_{h,sw}$.

The primary concentrators are protected from the elements within a building when the furnace is not in operation and visibly show little deterioration. D&S measurements on the concentrator surfaces also show only a small reduction in reflectivity at 650 nm. The Gier Dunkle instrument can not properly be used on a curved mirror surface; therefore, in Eq. 10, $\rho_{c,sw}$ is based on measurements from the D&S device only. We assign a value of 87.5% to $\rho_{c,sw}$.

Currently, we have limited reflectivity data and flux-map images which we can use to compare the BEAMCODE power estimates before and after CATARACT processing with theory. The results of two of the tests that we can compare are shown in Table 1. Percent difference in Table 1 is calculated as (Theoretical Power - BEAMCODE Power)/Theoretical Power.

These limited results indicate that the BEAMCODE images processed through CATARACT do agree more closely with the theoretical calculations. For these tests, however, all of the BEAMCODE power calculations are within the +/-4% measurement uncertainty we assign to the theoretical calculations.

We are examining new methods to quickly and accurately measure the solar weighted reflectivity of our heliostat and primary concentrator. We are also developing a steady-flow, cold-water calorimeter that is designed to have a measurement uncertainty of +/-2%. The calorimeter will be more accurate than either theoretical calculations or the flux-mapping system. The new calorimeter and reflectivity measurement methods will help us better characterize the performance of our furnace.

While the flow calorimeter will provide us with a better power measurement than the CATARACT-processed BEAMCODE images, it will not make the current flux-mapping system obsolete. The flux-mapping system's speed and ability to give both power calculations and flux distributions ensure that it will continue to be a useful tool. We anticipate performing a fairly rigorous comparison of power estimates from the flow

calorimeter, the flux-mapping system and theoretical calculations in the near future.

CONCLUSIONS

The scatter-plate flux-mapping system provides a quick, easy method to determine flux profiles and total power estimations at the HFSF. However, because of the furnace's unique geometry, the camera for the system must be located at an angle of 20° to the target plane. This angle introduces a systematic error into the flux profiles and the power calculations. Our computer code, CATARACT, successfully compensates for this angle to provide true shapes for the images and better estimates of the total power delivered to the target plane.

REFERENCES

Bingham, C. and A. Lewandowski, 1991, "Capabilities of SERI's High-Flux Solar Furnace," *Proceedings of the 2nd ASME-JSES-JSME International Solar Energy Conference*, Reno, NV.

Lewandowski, A., 1989, "The Design of an Ultra-High Flux Solar Test Capability," *Proceedings of the Intersociety Energy Conversion Engineering Conference, IECEC-89*, Washington, D.C.

Lewandowski, A., C. Bingham, J. O'Gallagher, R. Winston, and D. Sagie, 1991, "Performance Characteristics of the SERI High-Flux Solar Furnace", *Solar Energy Materials*, Vol. 24, pp. 550-563.

Masterson, K. and M. Bohn, 1982, "Scatterplate Flux Mapping for Solar Concentrators," Technical Report TR-255-1432, SERI, Golden, CO.